

Experimental and Numerical Study of Microcavity Filling Regimes for Lab-on-a-Chip Applications

Luise Nagel^{1,3}, Anja Lippert^{1*}, Ronny Leonhardt¹, Tobias Tolle¹,
Huijie Zhang^{2,3}, Tomislav Marić^{3*}

¹Corporate Research, Robert Bosch GmbH, Robert-Bosch-Campus 1, Renningen,
71272, Germany.

²Mobility Electronics, Robert Bosch GmbH, Markwiesenstrasse 46, Reutlingen,
72770, Germany.

³Mathematical Modeling and Analysis, Technical University of Darmstadt,
Peter-Grünberg-Str. 10, Darmstadt, 64287, Germany.

*Corresponding author(s). E-mail(s): anja.lippert@bosch.com;
maric@mma.tu-darmstadt.de;

Abstract

The efficient and voidless filling of microcavities is of great importance for Lab-on-a-Chip applications. However, predicting whether microcavities will be filled or not under different circumstances is still difficult due to the local flow effects dominated by surface tension. In this work, a close-up study of the microcavity filling process is presented, shedding light on the mechanisms of the filling process using experimental insights accompanied by 3D numerical simulations. The movement of a fluid interface over a microcavity array is investigated optically under consideration of different fluids, capillary numbers, and cavity depths, revealing a regime map of different filling states. Moreover, the transient interface progression over the cavities is analyzed with attention to small-scale effects such as pinning. Besides the visual analysis of the image series, quantitative data of the dynamic contact angle and the interface progression is derived using an automated evaluation workflow. In addition to the experiments, 3D Volume-of-Fluid simulations are employed to further investigate the interface shape. It is shown that the simulations can not only predict the filling states in most cases, but also the transient movement and shape of the interface. The data and code associated with this work are publicly available at Bosch Research GitHub [1] and at the TUDatalib data repository [2].

Keywords: Lab-on-a-Chip, Volume-of-Fluid, Microcavity, Multiphase, Contact angle

1 Introduction

Lab-on-a-Chip (LoC) systems are an important area of research in healthcare technology. Providing fast and automated molecular diagnostic assays through miniaturization, LoC technology makes it possible to perform personalized medical analysis at the point of care without the need of large laboratories or specially trained personnel. LoC systems exploit microfluidic processes for the transport of samples and reagents [3, 4]. A prominent example is the filling of microcavities with sample liquids. Microcavity arrays can be employed for the application of multiplex quantitative Polymerase Chain Reaction (qPCR) [5–7]. The aliquotation of the sample fluid into separate isolated nanoliter volumes allows for highly parallelized sample analysis. Further applications of microcavity arrays are the trapping and separation of cells from fluid samples [8, 9]. A prerequisite to the efficiency of these complex fluidic processes is the understanding of the underlying multiphase flow mechanisms during the filling process, as recently discussed in [10, 11].

Experimental work on this topic typically features the large-scale filling of arrays consisting of hundreds of cavities, as investigated in [12] and [13]. The local transient flow behavior, including the contact line pinning at sharp edges, and local deformation of the interface are not considered in these large-scale experiments. In [14], the filling efficiency of microcavities is investigated under consideration of different flow velocities, cavity geometries, and contact angles, focusing on the steady state after the liquid has passed the cavities. In addition to experiments, simulation results are shown in [14], indicating that simulations can complement experimental data by giving 3D insight additionally to the top-down 2D view acquired from experiments. However, the transient processes causing the different filling efficiencies are not investigated further. A closer look at the transient filling behavior is given for very specific geometries, such as in [15–18]. However, these insights are not generalizable to standard topologies such as circular cavities, which are the most common shapes in LoC applications.

In recent work [11], two scenarios of flow over microcavities are simulated. To stabilize parasitic currents, an artificial viscosity model is employed and validated in [11]. The present work extends [11] with further experimental and numerical studies of the cavity filling process.

In order for simulations to represent two-phase flow including wetting effects, a meaningful choice of the contact angle model is of high importance. The contact angle is the angle formed between the fluid interface and a solid surface. In the absence of external forces, an equilibrium contact angle θ_{eq} can be reached, which is rare in technical applications. In a system with a moving interface, the dynamic contact angle depends on the contact line speed as well as local effects such as roughness and chemical structure, as is well known since decades [19]. However, although many modeling approaches exist to describe the contact angle dynamics, as recently reviewed in [20], currently available models are still not predictive for a given material combination due to the combination of effects ranging from the molecular to the macroscopic scale. Furthermore, the implementation of a contact angle model into FVM simulations is not trivial and gives rise to a large number of approaches, as reviewed in [21]. The most straight-forward approach is to measure an apparent contact angle in experiments for a given velocity and providing it as a boundary condition in the simulations. This method, however, requires a high quality and reproducibility of the experimental measurements, which is not straightforward in dynamic cases, as recently discussed in [22].

This work presents a thorough close-up investigation of the microcavity filling process through experimental and numerical investigation. The main objective is to identify different filling regimes and the corresponding movement of the fluid interface. The question is: under which circumstances are cavities filled, not filled, or partially filled? To this end, experiments are performed to visualize

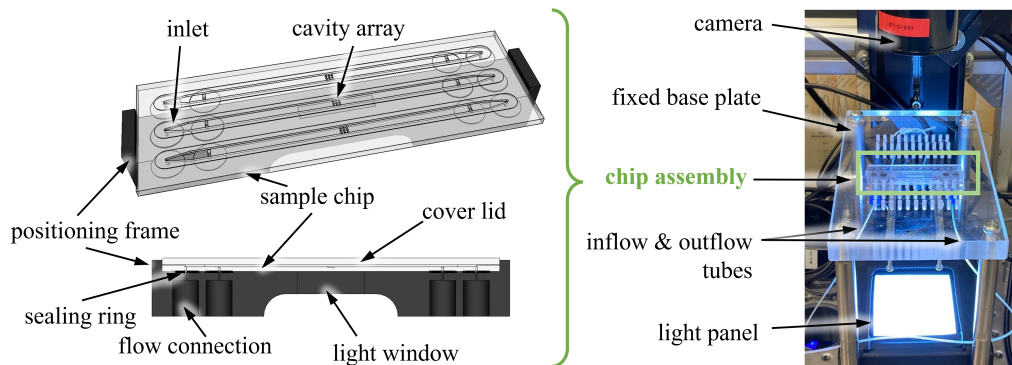


Fig. 1: Setup of the sample chip and the measurement system.

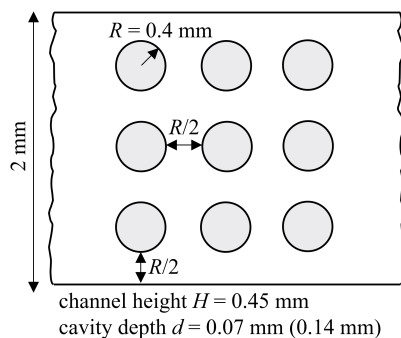


Fig. 2: Geometry and measurements of the cavity array.

the interface shape and movement in a setting of different fluids, velocities and geometries relevant for LoC applications. The experimental data is post-processed in an automated and thus reproducible workflow, yielding quantitative data for the interface movement and the dynamic contact angle. To complement the 2D experimental data, 3D simulations are performed. They are calibrated using the experimentally acquired contact angles. The simulations are compared to the experiments with regard to the filling regimes and interface progression, showing very good agreement and providing insight into the interface shape beyond the experimental view. The complete dataset and the postprocessing scripts are made publicly available at Bosch Research GitHub [1] and at the TUDatalib data repository [2].

2 Materials and Methods

2.1 Experimental Methods

2.1.1 Materials and Setup

The experimental setup is shown in fig. 1 and explained in detail in [11], a short summary is given in the following. The flow over microcavities is visualized using top-down camera recordings.

Table 1: Fluid parameters and surface tension coefficients in fluid-air at 20 °C temperature. Surface tension coefficient of Tween-80TMsolution - air was measured in-house.

Fluid	Density ρ (kg/m ³)	Dyn. viscosity μ (mPas)	Surface tension σ (mN/m)
Air [26]	1.19	0.0182	-
Water[26–28]	998.2	0.9982×10^{-3}	0.07274
Tween [®] -80 solution [23]	998.2	0.9982×10^{-3}	0.03500
Novec-7500 [29]	1614.0	1.2428×10^{-3}	0.01620

Table 2: Capillary numbers corresponding to the given velocities for each experimental case.

Velocity (m/s)	Ca Water	Ca Tween	Ca Novec
10^{-4}	1.37×10^{-6}	2.85×10^{-6}	
10^{-3}	1.37×10^{-5}	2.85×10^{-5}	
10^{-2}	1.37×10^{-4}	2.85×10^{-4}	7.67×10^{-4}
10^{-1}			7.67×10^{-3}

As test samples, polymethyl-methacrylate (PMMA) microscopy slides (Microfluidic ChipShop) are customized with open channels and cavities by micromilling. The resulting geometry and measurements are given in fig. 2. Two variants of the geometry are used, differing in the cavity depth. As a result of the micromilling, the sample roughness is in the scale of $\leq 5 \times 10^{-6}$ m. A smooth, transparent cover lid (Zeonex, Microfluidic Chipshop) is used to close the channels. The flow is controlled by a syringe pump, and a high-speed camera is used to record the flow over the microcavity array. The images are resolved with a pixel size of three micrometers. Three working fluids are employed: water, a 0.1 % Tween[®]-80 aqueous solution (Tween[®]-80, Croda International plc), and NovecTM 7500 (3MTM NovecTM 7500 Engineered fluid). The fluid properties are given in tab. 1. The Tween[®]-80 aqueous solution, hereafter referred to as Tween, is typically used as a buffer solution in LoC applications and differs significantly from water in the surface tension parameter [23–25]. NovecTM 7500, hereafter called Novec, which can be used as a sealing fluid in LoC microcavity arrays, exhibits very low surface tension. Furthermore, it shows perfect wetting on PMMA and Zeonex surfaces ($\theta_{eq} = 0$), whereas both other liquids are partially wetting ($\theta_{eq} > 0$). Four different volumetric flow rates are considered. The resulting flow velocities and capillary numbers Ca are given in tab. 2. The capillary numbers are in the range of $Ca = 10^{-6} \dots 10^{-3}$, which is the regime relevant for LoC applications. The investigation of lower capillary numbers and static contact angles in this setting is not feasible with satisfactory accuracy, since the interface movement appears instable and very sensitive to small roughness edges in the geometry.

2.1.2 Data Processing

Based on the recorded time series of the interface movement, three sets of information are derived: First, the filling regimes of the cavities, second, the dynamic contact angles upstream of the cavity array, and third, the quantitative interface progression over time. For the first task, a manual evaluation is sufficient, since only a qualitative analysis is necessary, see section 3.3. The workflow for the contact angle measurement and interface tracking is automated using Python. The automation

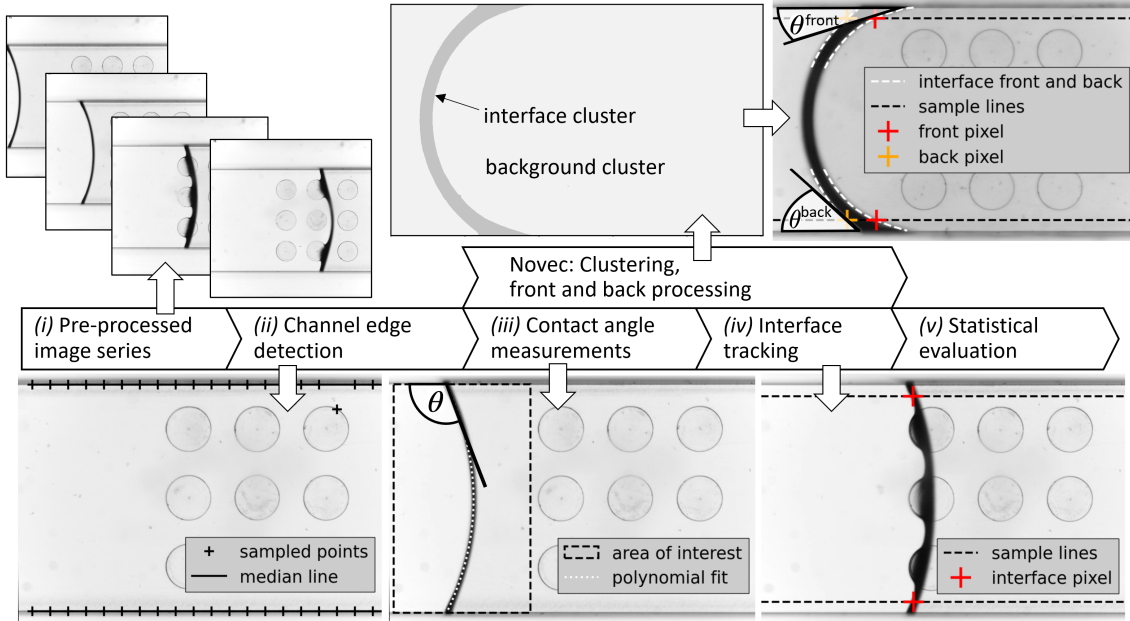


Fig. 3: Workflow of the experimental data processing.

provides a basis for standardized and reproducible measurements. It is presented in fig. 3 and published together with the complete dataset at [1, 2]. The processing steps are shortly described hereafter.

(i) Pre-processed image series. The only manual steps that need to be taken are the rotation of the datasets to ensure the horizontal alignment of the channel edges, and the definition of the x-position of the beginning of the cavity array, which is necessary for the contact angle detection. The cavity array is excluded of the contact angle measurements because influences of the local topology on the contact angles are expected in that area. These steps are carried out using the software ImageJ [30].

(ii) Channel edge detection. The horizontal channel edges, which appear dark in the images, are detected using the Python library opencv [31] and a sampling method. The lowest grayscale values (darkest pixels) across several vertical lines are sampled. The line positions are chosen such that the channel edges are known to be within the sampling range of the lines. The median of the x-positions of the sampled darkest pixels is considered the position of the channel edge. The choice of the median is, provided many sample lines, very robust against outliers.

(iii) Contact angle measurement. The contact angles are measured in a global approach. The whole interface, which appears dark in the images, is approximated with a polynomial fit. A polynomial degree of three is shown to be robust and to approximate the interface sufficiently well. The fitting is preceded by a simple filtering step to remove outliers, and is performed with the Random Sample Consensus (RANSAC) method [32] available in the scikit-learn library [33] which filters additional outliers. Once the polynomial representation of the interface is acquired, the contact angles at the channel bottom and top are easily computed from the slope at the edges of the interface.

(iv) *Interface tracking.* To quantify the interface progression, a point tracking is performed using the channel edge data resulting from step (ii). At each time step, the darkest pixel across two horizontal lines is detected. The lines are located at a distance of 0.1 mm from the channel walls, at the center between the respective channel wall and the adjacent cavity row. This position is chosen as a compromise between closeness to the cavities and robustness of the algorithm, since the tracking of the interface directly at a cavity is prone to sampling errors due to cavity edges appearing as dark regions in the image.

(v) *Statistical evaluation.* The measured contact angles are collected for all time steps in each measurement. This large dataset is evaluated in box plots that show the measurement distributions. The results are discussed in section 3.1.1. Furthermore, the accuracy of the fitting algorithm in step (iii) is evaluated via the distance between the sample point inliers and the resulting fit curve. See fig. A1 in the appendix for further details.

2.1.3 Additional Post-processing for Interface with Low Contact Angle

In experiments with Novec, the low contact angles result in increased interface thickness due to 3D effects. Consequently, the default interface detection and tracking algorithms (iii, iv) yield high uncertainties, which require alternative post-processing steps. First, the interface is extracted using the clustering algorithm KMeans [33] which separates the image into two clusters: the interface and the background. Next, the interface front and back are identified from the cluster. Since the shape of the front and the back differ, the contact angles for both are acquired. To account for the elongated front, only the wall-adjacent pixels are used for the polynomial fit. Further details and all fitting parameters are documented in the code published at [1, 2].

2.2 Simulation Methods

2.2.1 Mathematical and Numerical Modeling

The simulations are performed with the plicRDF-isoAdvection geometrical unstructured Volume-of-Fluid (VOF) method [34–36]. The reader is directed to a review of unstructured geometrical VOF methods for more details [37]. As numerical framework, the open-source finite volume library OpenFOAM-v2212 [38] is used. Specifically, the employed solver is interFlow, part of the OpenFOAM-based TwoPhaseFlow framework introduced in [39, 40]. The case setup is publicly available at [1, 2].

2.2.2 Setup

The geometry used in the simulations is identical to the experimental geometry given in fig. 2, with the channel length adapted to the necessary length to represent the different contact angles. An xz -symmetry plane is employed to reduce the computational domain. It is realized with a free slip condition for the velocity, a zero-gradient condition for pressure and a constant contact angle $\theta = 90^\circ$. To ensure the validity of this boundary condition, selected cases were simulated with the full geometry, confirming that the filling behavior is not significantly influenced by the symmetry plane. For brevity, these results are not shown here. A constant velocity block-profile is given at the inlet, and the outlet is defined as a zero-pressure boundary. At the wall boundaries, a partial slip condition is used for the velocity, where the slip length is arbitrarily chosen as $\lambda = 0.02$ mm.

The unstructured mesh of the domain is created with `snappyHexMesh` and described in section 3.2. The time step for all cases is set to the capillary time step restriction

$$\Delta t < \sqrt{\frac{(\rho^- + \rho^+)(\Delta x)^3}{4\pi\sigma}}, \quad (1)$$

where ρ^\pm are the densities of the two fluids and Δx is the mesh resolution, as discussed in [41]. In the considered regimes, the capillary time step criterion is stricter than the CFL criterion. To increase the simulation robustness, an artificial interface viscosity and a wisp filtering method are used, which are discussed and validated in detail in previous work [11]. The chosen artificial viscosity is $\mu_\Sigma = \mu$, and the wisp tolerance is $\varepsilon_w = 10^{-5}$. A constant contact angle θ is defined at the walls, corresponding to the apparent contact angles measured in the experiments (section 3.1, fig. 4). The dynamic contact angle of the fluid to the cover plate material (Zeonex) is not directly detectable in this study. For water and Tween, the equilibrium contact angle with Zeonex measured with standing droplet experiments is used instead. For water, it equals $\theta = (94 \pm 5)^\circ$ and is in agreement with literature data [42–44]. For Tween, the measured static contact angle is $\theta = (85 \pm 5)^\circ$. For Novec, the static contact angle equals zero, therefore the contact angle is assumed to depend on the velocity in the same way as for the PMMA material. The results presented in section 3.3 show that these assumptions yield a good match to the experimental results.

3 Results and Discussion

3.1 Dynamic Contact Angles

3.1.1 Experimentally Acquired Contact Angles

In fig. 4 the dependency of the apparent contact angles on the given capillary numbers $Ca = \mu U / \sigma$ is shown as a box plot. The values of the contact angles result directly from the automated data processing workflow described in section 2.1.2, including the measurements at the top and the bottom for three repetitions for all cases. A strong dependency of the contact angle on the capillary number is visible for all fluids, with the median contact angle increasing by more than ten degrees in the range of the given capillary numbers. The inter-quartile box representing the middle 50% of the data spans over less than seven degrees, indicating that the medians represent the data sufficiently well. For water and Tween, large outliers are visible in cases with apparent contact angles slightly above $\theta = 90^\circ$. In this contact angle range, the interface appears very thin in the images, which reduces the detection accuracy. For Novec, outliers occur at the highest capillary number, especially at the interface front, which can be attributed to single images in which small errors in the clustering step yield large approximation errors of the interface shape. In general, the overall number of outliers is deemed acceptable for such a large dataset. It should be noted that the local velocity in the vicinity of the wall can be expected to be slightly lower than the given mean velocity U due to wall friction. This influence is regarded as minor and subsequently neglected in this study.

3.1.2 Contact Angle Calibration for Simulation

For water and Tween, the medians presented in fig. 4 are used as constant contact angle boundary conditions in the simulations. Since the pixel size of the images $x_p = 0.003$ mm is only one order of magnitude below the computational grid size $\Delta x = 0.033$ mm, it is assumed that the measured

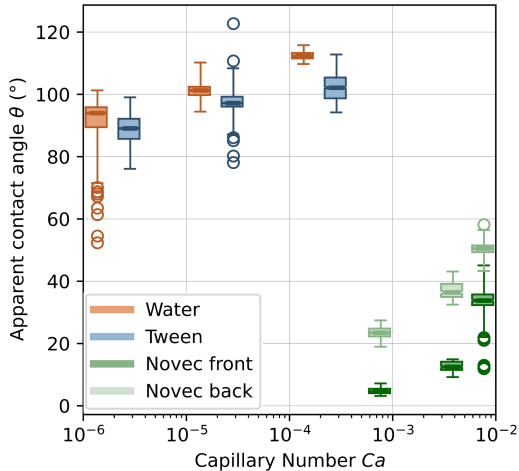


Fig. 4: Measured apparent contact angles for the considered fluids. The horizontal lines show the median, the boxes represent the middle 50% of the data. The whiskers extend from the box to the respective farthest data point lying within $3 \times$ the height of the box, the circles represent outliers.

apparent contact angles are suitable for this use. For Novec, the interface exhibits different apparent contact angles at the front and the back, respectively. This raises the question of which contact angle should be chosen in the simulation to represent the experimental data. Here, this question is answered using a line-search parameter study. Different contact angles in the simulations are tested to find the best match to the experiments. To achieve an appropriate comparison, the simulation data is postprocessed with the same algorithm as the experimental images, cf. section 2.1.3. To get a matching representation of simulation and experiment, the experimental view is reproduced using a 2D projection of the reconstructed interface in ParaView [45], as shown in fig. 5. Simulations of a flow in the channel, excluding the cavities, are carried out with different contact angles. The resulting measured contact angles, which may deviate from the given boundary conditions, are compared to the respective experimental values. The graphs in fig. 5 show the results for Capillary numbers $Ca = 7.67 \times 10^{-3}$ and $Ca = 7.67 \times 10^{-4}$. It is apparent that the measured contact angle does not necessarily match the prescribed contact angle. Apart from the uncertainties induced by the 2D projection and the image processing workflow, which are assumed to be in the order of up to five degrees, a further source of uncertainty is the implementation of the contact angle boundary in the simulation framework. As recently discussed in [46], the contact angle is considered indirectly in the interface reconstruction instead of being explicitly prescribed, which gives rise to inaccuracies especially for very high or very low contact angles. To identify the simulation that matches the experimental data sufficiently, the average of the front and back contact angles are used.

For $Ca = 7.67 \times 10^{-3}$, the simulation with the prescribed contact angle $\theta = 45^\circ$ matches the experimental results best. The corresponding shape of the interface (fig. 5 left) shows a good match between simulation and experiment, confirming that the chosen contact angle is suitable.

For $Ca = 7.67 \times 10^{-4}$, the measured contact angles deviate stronger from the given contact angles. This can be explained by the long rivulets exhibited at the channel edges, which pose a challenge not only for the interface reconstruction in the simulation, but also for the image processing algorithm. Especially in the experimental images, the tips of thin rivulets are difficult to distinguish

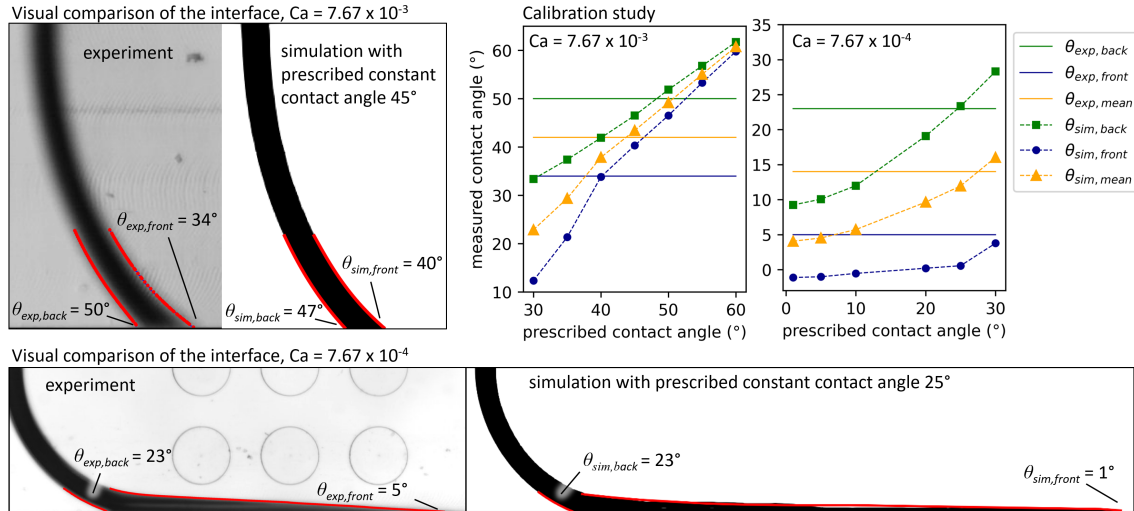


Fig. 5: Contact angle calibration for Novec. Top left, bottom: Interface shape and contact angles in experiment and selected simulation cases for different capillary numbers. Top right: results of the calibration study.

from the wall in the grayscale images due to limited resolution. Moreover, the rivulet shape depends strongly on the edge geometry, and while a perfect 90° wall angle is used in the simulations, the experimental geometry might deviate slightly, adding another source of uncertainty. Generally, the formation of rivulets during forced wetting in rectangular channels is an active research topic in itself (cf. [47, 48]) and an in-depth analysis of their length and shape is out of scope of this work. Instead, the focus here is on establishing a suitable contact angle for the simulations, which is in the range of $\theta = 25 \dots 30^\circ$ according to the graph in fig. 5. The visual comparison of the experiment and the simulation with $\theta = 25^\circ$ (fig. 5 bottom) shows a reasonable match of the interface shape with the exception of the rivulet length. For the following sections, the contact angle $\theta = 28^\circ$ is chosen as a compromise between the two most promising contact angles $\theta = 25^\circ$ and $\theta = 30^\circ$.

To test the robustness of the presented results, the dependency of the measured contact angles on mesh resolution, artificial viscosity, and slip length is shortly discussed in the appendix in section A.2.

3.2 Mesh Refinement Study

To test the dependency of the results with regard to increasing mesh resolution, two cases are considered which represent different filling regimes. Three different mesh resolutions are considered, with cell lengths $\Delta x = (0.033, 0.02, 0.01)$ mm. As means of comparison, the interface movement at different positions is used. The results are presented in fig. 6, where the schemes on the right show the measurement positions. In the left plot in fig. 6, the result for the case with the fluid combination Novec-air at $Ca = 7.67 \times 10^{-4}$ is displayed. In this case, the cavities are filled, as discussed later in section 3.3.2. The interface is tracked directly above the cavities at $z = z_1 = 0.001$ mm across three different positions $y_{1,2,3} = (0.0001, 0.1, 10)$ mm which are indicated by the colors in the scheme. The three different meshes are shown with different line styles. It is visible that the interface

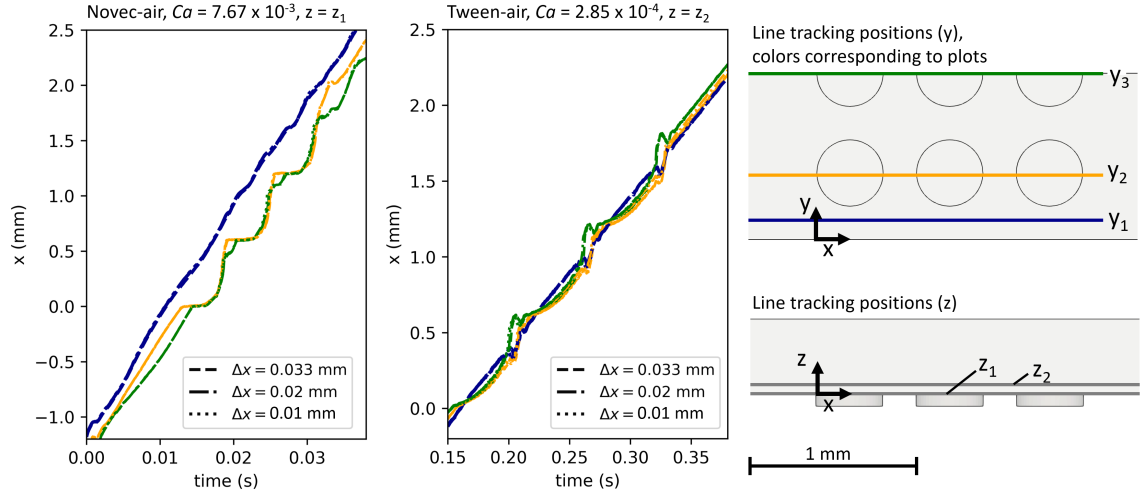


Fig. 6: Interface tracking results for three mesh refinement steps. Left and center: results for two different cases. Right: scheme showing the tracking positions.

movement at the different y positions differ significantly, but the difference between the resolutions is indistinguishable in comparison. The same holds for the second case (Tween-air at $Ca = 2.85 \times 10^{-4}$) which is shown in the right plot. Here, the cavities are not filled, as discussed later in section 3.3.3. In this scenario, the interface is tracked above the cavities at $z = z_2 = 0.05$ mm to exclude the impact of the interface pieces separating at the top of the cavities. The interface movement across several y positions does not differ strongly, and the changes in the mesh resolution do not influence the progression significantly. As a result of these studies, the mesh resolution $\Delta x = 0.033$ mm is chosen for all following simulations as a compromise between computational resources and a well-resolved interface.

3.3 Cavity Filling Regimes

3.3.1 Regime Distinction

When the interface passes the cavities, three scenarios are possible. Examples are depicted in fig. 7, where the regimes are differentiated as follows:

- Filled (F), fig. 7a: During the filling process, the interface firstly pins at the cavity edges, and subsequently moves through the cavities. All nine cavities are filled with the fluid, in some cases leaving tiny air bubbles at the cavity bottoms.
- Not Filled (N), fig. 7b: Pinning is observed at the cavity edges, and the interface moves over the cavities, leaving behind air cushions. No cavity is fully filled.
- Partially Filled (P), fig. 7c: Some of the cavities are fully filled, while air cushions or large bubbles remain in some other cavities.

To determine whether the cavity array is filled, partially filled, or not filled, the image sequence is interpreted with regard to the movement of the interface and the state of the cavities after the

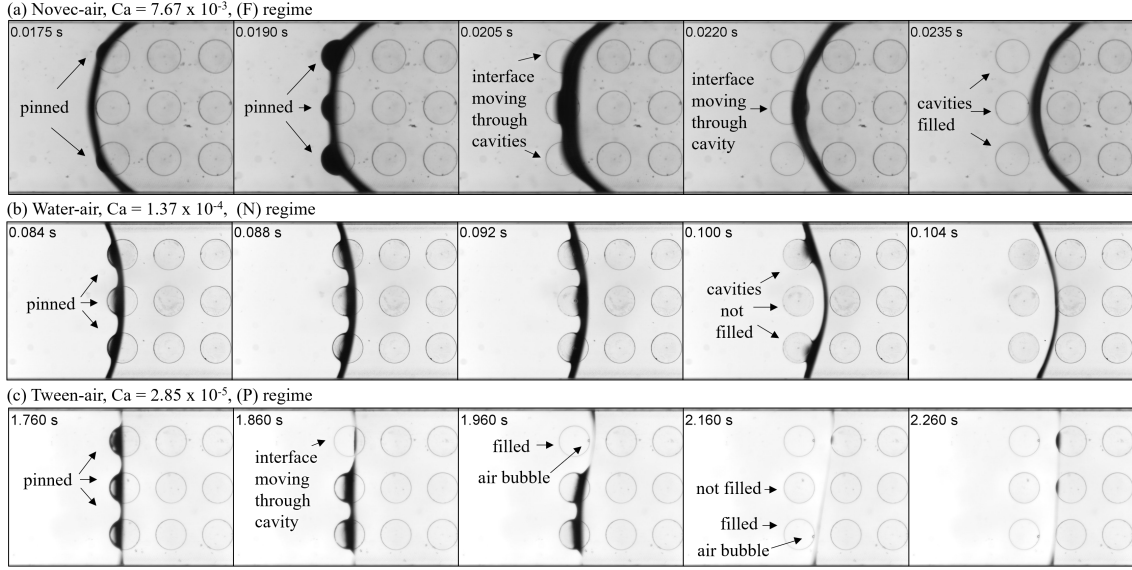


Fig. 7: Examples of the interface movement with different fluids and velocities.

interface has passed. All experiments are performed three times to ensure reproducibility, and the filling regimes are confirmed in the repeated measurements.

3.3.2 (F) Regime - Complete Cavity Filling

In (fig. 7a) the (F) regime is depicted for the experiment with Novec at $Ca = 7.67 \times 10^{-3}$. It is characterized by the interface firstly pinning at the cavity edges before traversing them.

A more close-up look at the filling is given in fig. 8 for the experiment with Novec at $Ca = 7.67 \times 10^{-4}$. In the experimental images (fig. 8 left) the interface appears thick, and rivulets are visible at the walls due to the low contact angle. Four time steps are shown which represent critical steps during the filling process. Firstly, the interface pins at the edges of the first cavity ($t = 0.16$ s). Next, within approximately 0.015 seconds, the near-wall cavities are filled ($t = 0.175$ s). Afterwards, the interface pins strongly at the center cavity ($t = 0.19$ s) and traverses it ($t = 0.2$ s). This highly dynamic process is confirmed by the simulation results (fig. 8 center). The 3D view reveals that the interface is strongly curved across the y axis, therefore appearing very thick in the top-down view.

For a quantitative analysis of the filling process, interface tracking plots are used (fig. 8 right). The experimental results are given in terms of the interface front and back pixels that are identified as discussed in section 2.1.3, the measurements being limited by the size of the field of view spanning two millimetres. Two positions are considered for the interface tracking: $y = y_1 = 0.7$ mm between two cavity rows, and $y = y_2 = 0.1$ mm between the lower cavity row and the wall. The results are given as solid lines in the graphs. It is apparent that at y_1 , the front and back are close to each other, whereas at y_2 , they are approximately one millimeter apart, which represents the long rivulets at the channel edges. Furthermore, kinks can be seen in the interface progression at both positions. The times at which these kinks appear match the pinning and filling steps visualized in fig. 8 left. To compare the numerical results to the experiment, the same y positions are used

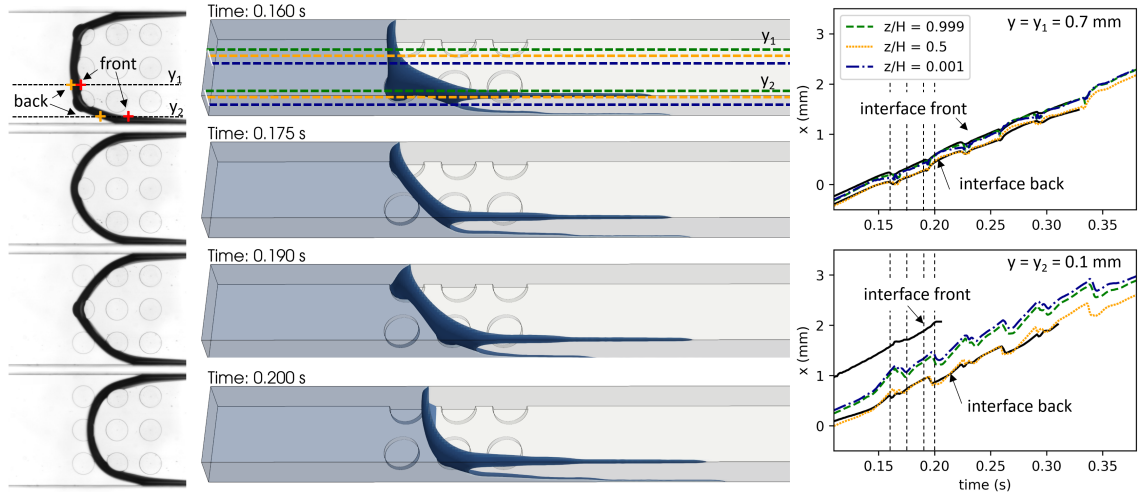


Fig. 8: Interface tracking results for (F) regime, fluid pairing Novec-air, $Ca = 7.67 \times 10^{-3}$. Left: experimental view, center: simulation results including positions of the tracking lines, right: interface tracking plot at two y positions.

for interface tracking in the simulation. Additionally, the 3D results allows for a tracking along different heights z , which are represented by different colors in the graph. At y_1 , the simulation results show a very close match to the experiment, including the kinks. At y_2 , a discrepancy is visible between simulation and experiment. The simulation result at $z/H = 0.5$ matches the back of the experimental interface. In the 3D view, this corresponds to the center of the interface which lags behind the edges due to the low contact angle. With this reasoning, the experimental interface front is expected to match the simulation at $z/H = 0.001$ and $z/H = 0.999$, since the wall-near interface represents the front. However, while the trend in the lines is correct, a good match is not achieved. This can be attributed to the difficulties in correctly representing rivulet length and shape, as discussed in section 3.1.2. Due to the good match of the other characteristics and the filling state, which remains the main focus in this study, the results are considered satisfactory.

3.3.3 (N) Regime - No Cavity Filling

In the (N) regime (fig. 7b), the interface pins at the cavity edges, and moves over the cavities. No snapping movement through the cavities is observed, and air bubbles remain in the cavities, covered by the fluid. It should be noted that the interface covering the cavities is parallel to the camera plane, and is therefore detectable only due to a minor decrease in brightness. The process of pinning and detachment can occur symmetrically to the channel center line, but in some repetitions, the interface at one wall proceeds the movement of the opposite side, which can be the cause of minor differences in roughness or contamination. A further observation is that the experiments with Tween, the air cushions tend to change shape to a more spherical bubble over time. The details of this process cannot be investigated within the scope of this work, however, a possible explanation is the transient behavior of the surfactant distribution along the interface. Fig. 9 presents the similar case of the flow of Tween at $Ca = 2.85 \times 10^{-4}$, along with the comparison to simulation results. The visual comparison of the interface movement over the first cavity row is shown at the left and

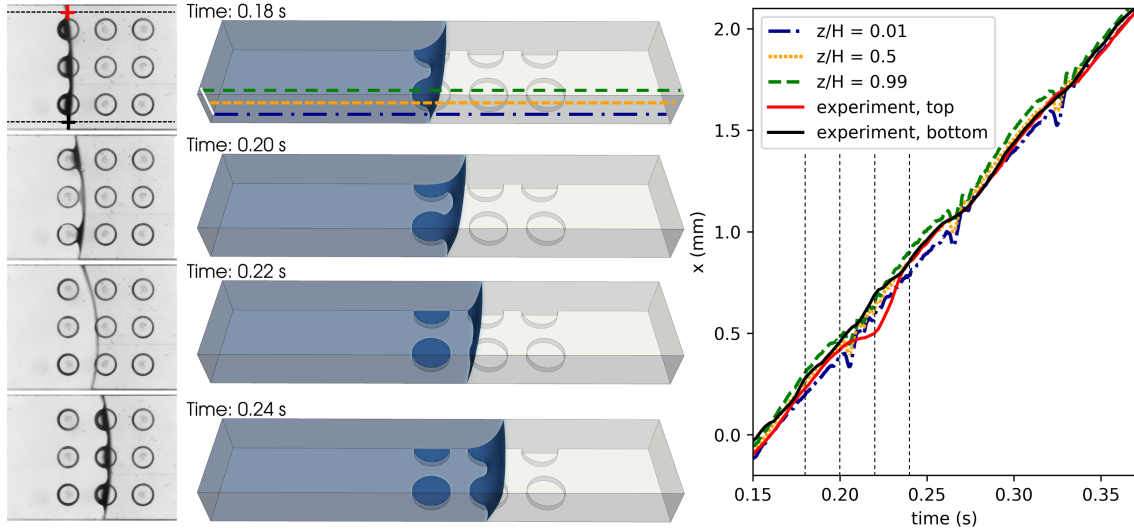


Fig. 9: Interface tracking results for (N) regime, fluid pairing Tween-air, $Ca = 2.85 \times 10^{-4}$. Left: experimental view, center: simulation results including positions of the tracking lines, right: interface tracking plot.

center of fig. 9. The pinning of the interface ($t = 0.08$ s) is succeeded by the detachment in the center cavities ($t = 0.10$ s) and the wall-adjacent cavity ($t = 0.12$ s). The quantitative comparison of the interface movement is shown on the right side of fig. 9. The experimental results are displayed for the top and bottom interface movement, corresponding to the positions given on the top left picture of fig. 9. It can be observed that the interface movement is relatively uniform with the exception of the time span $t = 0.1$ s $\leq t \leq 0.14$ s. As seen in the visual depictions, this time span corresponds to the interface moving over the first cavity row. In the experiment, the interface detaches slightly earlier at the bottom cavity than the top cavity, resulting in an asymmetric shape, visible at $t = 0.12$ s. This causes the splitting of the top and bottom curves in the interface tracking plot. However, for the second and third cavity row, the interface tracking is more uniform, only showing slight waves when the cavities are passed, signifying a symmetrical interface shape.

In the simulations, the general movement is confirmed. Kinks in the interface progression are visible at the times where the cavity rows are passed, showing an oscillation when the air cushions are created and the interface breaks up into separate parts. These oscillations occur slightly earlier than in the experimental curve, signifying a minor difference in the timing of the interface separation. Furthermore, the asymmetric interface movement of the experiments at $t = 0.1$ s $\leq t \leq 0.14$ s cannot be recreated in the simulations. Besides this, the experimental results are very well matched.

3.3.4 (P) Regime - Partial Cavity Filling

In the (P) regime (fig. 7c) the exact movement of the interface and the number of filled cavities are not directly reproducible between repeated experiments. The filling process in this regime is strongly depending on small local effects such as pinning on rough edges. In this regime, the simulation results deviate from the experimental data. The local deviations from the idealized sharp-edge geometry cannot be represented in the simulations, and the simulation yields a (N) regime. One further aspect

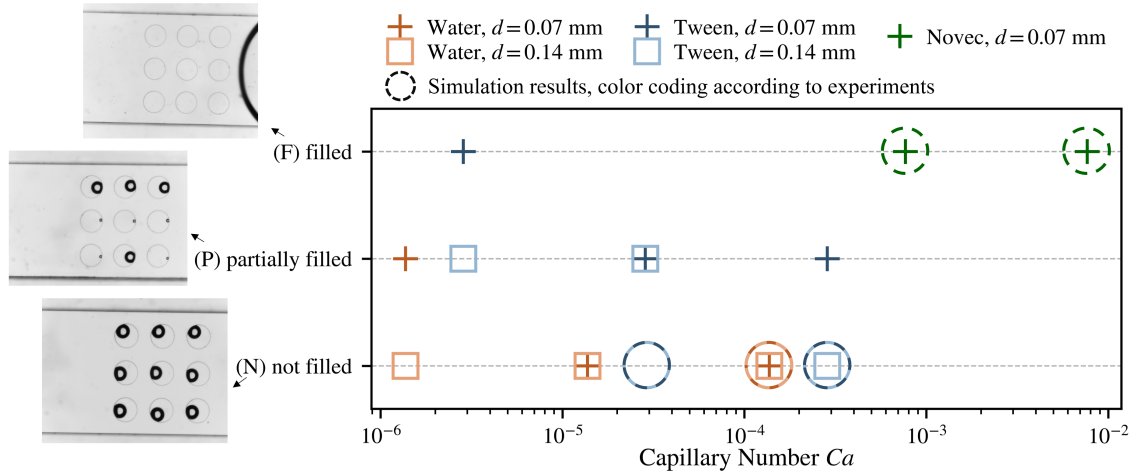


Fig. 10: Experimentally acquired filling regimes. Simulation results given for comparison.

to consider is the effect of the dynamic contact angle. In the simulation, the velocity dependence of the contact angle is not captured, which is also a possible explanation for the discrepancies. To put the (P) regime into context, it should be noted that partial filling is not desired in LoC applications. The appearance of even a few small air pockets in large-scale microcavity arrays can compromise the accuracy of the biochemical processes. Therefore, the tendency of the simulation towards predicting the (N) regime can be considered as a conservative prediction with regard to the filling state. This is a positive aspect for future exploratory studies using simulations.

3.3.5 Regime Map

To summarize the results, fig. 10 displays the filling regimes acquired in all experiments. The filling states are presented for different fluids, capillary numbers, and, for Tween and water, different cavity depths. The experiments with Novec result in the (F) regime in all cases. It can be assumed that for lower capillary numbers, the (F) regime is also achieved since capillary forces will dominate even stronger and the contact angle will be reduced even further. In the experiments with Tween, different regimes are observed depending on the capillary number and the cavity depth. The experiments show that increasing capillary numbers result in an overall lower chance of filling. This can be attributed to the decrease of importance of capillary force, and to the increasing contact angles with increasing capillary number, as seen in fig. 4. Furthermore, the deep cavities ($d = 0.14$ mm) are less likely to be filled than the shallow cavities ($d = 0.07$ mm). This result is intuitive and matches the findings in [14]. The experiments with water yield the (N) regime in all but one scenario. The high contact angle prevents the filling, and only the lowest capillary number results in a partial filling in the shallow cavities.

In addition to the experimental data, fig. 10 gives an overview of the simulation results. Not all capillary numbers are considered in the simulations, since simulations with low capillary numbers ($Ca < 10^{-5}$) show poor stability due to high parasitic currents. In the considered range of capillary numbers, the simulations match the experimentally acquired regimes very well for the (F) and (N) cases, as discussed in section 3.3.2 and section 3.3.3. The (P) regime is not achieved in any of

the simulations due to the reasons discussed in section 3.3.4. In general, the agreement between simulations and experiments is very satisfactory, showing that simulation can be used to investigate filling regimes. Moreover, the simulations provide 3D insights into the interface shape and movement, which cannot be achieved in the top-down view of the experiments, and therefore help to explain the experimentally achieved results.

4 Summary and Conclusion

Understanding the mechanisms of a fluid interface traversing over microcavities is vital for improving the efficiency of microcavity filling for LoC applications. This work presents a close-up experimental investigation of filling regimes of a 3×3 microcavity array with various fluids and capillary numbers. The apparent dynamic contact angles and interface movements are acquired with an automated image processing workflow, ensuring reproducible results, and providing calibration data for simulations. The close-up investigation of the experimental interface movement during different filling scenarios reveals different mechanisms for the filling versus not filling states.

Furthermore, it is shown that the simulation using the geometrical unstructured VoF method can predict the filling behavior for filled and not filled cavities. The third regime that is observed in the experiments, where only a part of the cavities is filled, cannot be recreated by the simulations. In this regime, the filling state depends heavily on minor geometry kinks, transient surfactant distribution, or contaminations, which cannot be represented in the simulations. Since partial filling is not desired in LoC applications, the tendency of the simulation towards not filling the cavities is desirable. The fact that simulations can predict the filling state across a range of capillary numbers and contact angles is a promising finding. The 3D insights into the interface shape acquired in the simulations complement the 2D experimental data. In future work, such simulations can be used to perform shape optimizations and large parameter studies that would be very costly to perform experimentally. Furthermore, additional effects such as species transport can be investigated in future work to shed more light on reactive multiphase flows occurring in LoC systems.

5 Acknowledgments

The authors would like to thank Dr. Mathis Fricke from Technical University Darmstadt for the helpful and valuable discussions on contact line physics.

The last author acknowledges the funding by the German Research Foundation (DFG): July 1 2020 - 30 June 2024 funded by the German Research Foundation (DFG) - Project-ID 265191195 - SFB 1194.

Appendix A

A.1 Accuracy of Polynomial Fit in the Interface Detection Method

To test the accuracy of the polynomial fit applied to the interface shape, the root-mean-square distance x_{RMS} between the inliers of the RANSAC method and the resulting polynomial is computed

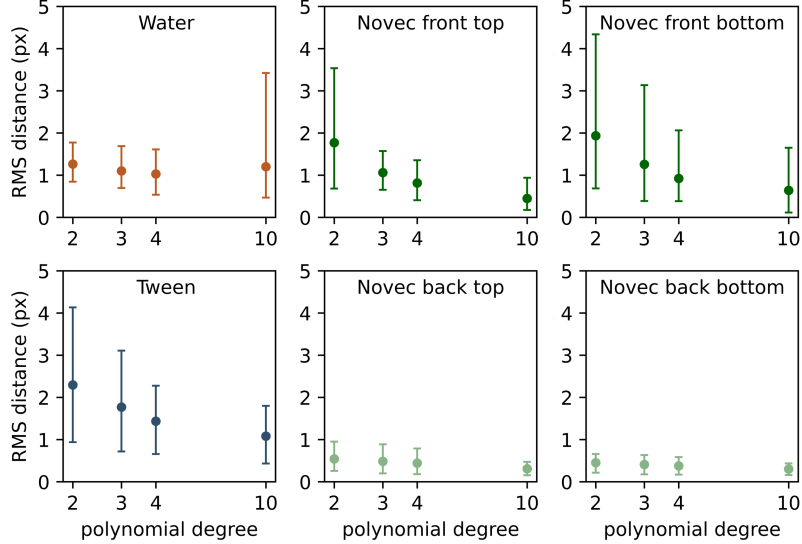


Fig. A1: Distance between sampled inlier points and polynomial fit in interface detection for all considered fluids.

for all images of each case as

$$\mathbf{x}_{RMS} = \frac{1}{N_{img}} \sum_{N_{img}} \left[\sqrt{\frac{1}{N_{in}} \sum_{N_{in}} ((x_{in} - x_{fit})^2)} \right], \quad (\text{A1})$$

where the index in refers to the inliers, img refers to the images, and x_{fit} indicates the points of the polynomial fitting curve. To test the influence of the polynomial degree used for curve fitting, four different polynomial degrees are compared. Fig. A1 shows the result for all considered fluids as error bar plots, in which the dots signify the average and the bars signify the maximum and minimum values. For Novec, the interface is fitted separately at different positions, therefore the respective results are given in separate plots. It can be seen that the fitting accuracy is within five pixels in all cases. Since the influence of the polynomial degree is sufficiently small, the choice of a third degree polynomial for all measurements is justified.

A.2 Contact Angle Calibration Study

To extend the results presented in section 3.1.2, the sensitivity of the contact angle calibration with respect to different parameters is shortly discussed here. Fig. A2 shows the calibration study results for Novec at $Ca = 7.67 \times 10^{-3}$ in three configurations: With increased mesh resolution ($\Delta x = 0.01$ mm), without artificial viscosity ($\mu_{\Sigma} = 0 \mu$), and with a no-slip boundary condition at the walls ($\lambda = 0$ mm), respectively. For the cases with $\Delta x = 0.01$ mm and $\mu_{\Sigma} = 0$, only slight deviations in the measured contact angles are visible compared to the graph in fig. 5. These deviations of up to five degrees are in the order of magnitude of the general uncertainty of the method, and are therefore not considered significant. In the case of $\lambda = 0$ mm, the measured contact

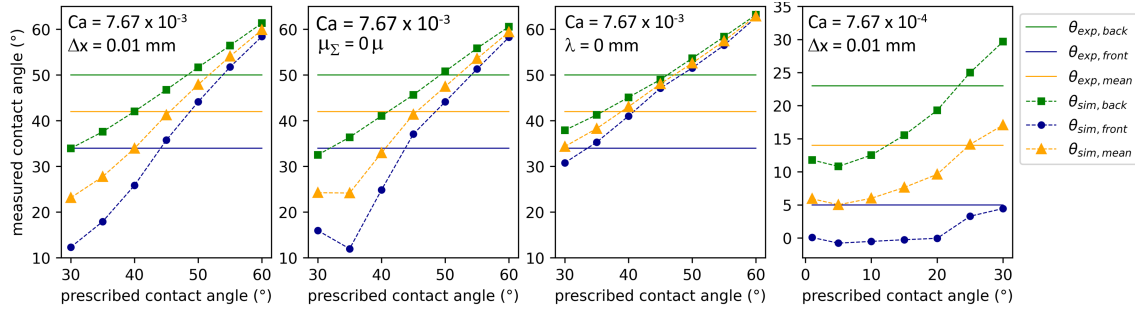


Fig. A2: Contact angle calibration study with respect to different simulation parameters.

angles are closer to the prescribed contact angles and generally higher than for $\lambda = 0.02$ mm as used in section 3.1.2. This shows that the slip length significantly influences the apparent contact angle in the simulation, and care should be taken in the calibration to account for the chosen slip length. A further investigation of this effect is planned in future work. However, the average apparent contact angle which matches the experimental value best $\theta = 40^\circ$, is still within five degrees of the originally established value $\theta = 45^\circ$ presented in section 3.1.2, and therefore acceptable.

The rightmost figure in fig. A2 presents an additional graph for Novec at $Ca = 7.67 \times 10^{-4}$ with increased mesh resolution ($\Delta x = 0.01$ mm). In comparison to fig. 5, the result confirms the low mesh dependency of the measured contact angles previously discussed for $Ca = 7.67 \times 10^{-3}$.

References

- [1] Robert Bosch GmbH. BoschResearch/sepMutliphaseFoam, git tree/publications/MicrocavityFilling. <https://github.com/boschresearch/sepMultiphaseFoam/tree/publications/MicrocavityFilling> (2024). Created: 2024-07-25.
- [2] Nagel, L. *et al.* Experimental and numerical study of microcavity filling regimes for lab-on-a-chip applications - data (2024-07-24). URL <https://tudatalib.ulb.tu-darmstadt.de/handle/tudatalib/4294>.
- [3] Pandey, C. M. *et al.* Microfluidics Based Point-of-Care Diagnostics. *Biotechnology Journal* **13**, 1700047 (2018). URL <https://onlinelibrary.wiley.com/doi/10.1002/biot.201700047>.
- [4] Niculescu, A.-G., Chircov, C., Bîrcă, A. C. & Grumezescu, A. M. Fabrication and Applications of Microfluidic Devices: A Review. *International Journal of Molecular Sciences* **22**, 2011 (2021). URL <https://www.mdpi.com/1422-0067/22/4/2011>.
- [5] Morrison, T. *et al.* Nanoliter high throughput quantitative PCR. *Nucleic Acids Research* **34**, e123–e123 (2006). URL <https://academic.oup.com/nar/article-lookup/doi/10.1093/nar/gkl639>.
- [6] Ahrberg, C. D., Lee, J. M. & Chung, B. G. Microwell Array-based Digital PCR for Influenza Virus Detection. *BioChip Journal* **13**, 269–276 (2019). URL <http://link.springer.com/10.1007/s13206-019-3302-8>.

- [7] Podbiel, D., Laermer, F., Zengerle, R. & Hoffmann, J. Fusing MEMS technology with lab-on-chip: nanoliter-scale silicon microcavity arrays for digital DNA quantification and multiplex testing. *Microsystems & Nanoengineering* **6** (2020). URL <https://www.nature.com/articles/s41378-020-00187-1>.
- [8] Rettig, J. R. & Folch, A. Large-Scale Single-Cell Trapping And Imaging Using Microwell Arrays. *Analytical Chemistry* **77**, 5628–5634 (2005). URL <https://pubs.acs.org/doi/10.1021/ac0505977>.
- [9] Yin, J., Deng, J., Du, C., Zhang, W. & Jiang, X. Microfluidics-based approaches for separation and analysis of circulating tumor cells. *TrAC Trends in Analytical Chemistry* **117**, 84–100 (2019). URL <https://linkinghub.elsevier.com/retrieve/pii/S0165993619301955>.
- [10] Podbiel, D., Zengerle, R. & Hoffmann, J. An analytical model for void-free priming of microcavities. *Microfluidics and Nanofluidics* **24** (2020). URL <http://link.springer.com/10.1007/s10404-020-2318-7>.
- [11] Nagel, L. *et al.* Stabilizing the unstructured Volume-of-Fluid method for capillary flows in microstructures using artificial viscosity. *Experimental and Computational Multiphase Flow* **6**, 140–153 (2024). URL <https://link.springer.com/10.1007/s42757-023-0181-y>.
- [12] Liu, H.-B. *et al.* Rapid distribution of a liquid column into a matrix of nanoliter wells for parallel real-time quantitative PCR. *Sensors and Actuators B: Chemical* **135**, 671–677 (2009). URL <https://linkinghub.elsevier.com/retrieve/pii/S0925400508006874>.
- [13] Cui, X. *et al.* A facile and rapid route to self-digitization of samples into a high density microwell array for digital bioassays. *Talanta* **233**, 122589 (2021). URL <https://linkinghub.elsevier.com/retrieve/pii/S0039914021005105>.
- [14] Padmanabhan, S. *et al.* Enhanced sample filling and discretization in thermoplastic 2d microwell arrays using asymmetric contact angles. *Biomicrofluidics* **14**, 014113 (2020). URL <http://aip.scitation.org/doi/10.1063/1.5126938>.
- [15] Sposito, A. J. & DeVoe, D. L. Staggered trap arrays for robust microfluidic sample digitization. *Lab on a Chip* **17**, 4105–4112 (2017). URL <http://xlink.rsc.org/?DOI=C7LC00846E>.
- [16] Lin, B. *et al.* A scalable microfluidic chamber array for sample-loss-free and bubble-proof sample compartmentalization by simple pipetting. *Lab on a Chip* **20**, 2981–2989 (2020). URL <http://xlink.rsc.org/?DOI=D0LC00348D>.
- [17] Quan, P.-L., Alvarez-Amador, M., Jiang, Y., Sauzade, M. & Brouzes, E. Robust and rapid partitioning in thermoplastic. *The Analyst* **149**, 100–107 (2024). URL <http://xlink.rsc.org/?DOI=D3AN01869E>.
- [18] Cohen, D. E., Schneider, T., Wang, M. & Chiu, D. T. Self-Digitization of Sample Volumes. *Analytical Chemistry* **82**, 5707–5717 (2010). URL <https://pubs.acs.org/doi/10.1021/ac100713u>.

- [19] de Gennes, P. G. Wetting: statics and dynamics. *Reviews of Modern Physics* **57**, 827–863 (1985). URL <https://link.aps.org/doi/10.1103/RevModPhys.57.827>.
- [20] Mohammad Karim, A. & Suszynski, W. J. Physics of Dynamic Contact Line: Hydrodynamics Theory versus Molecular Kinetic Theory. *Fluids* **7**, 318 (2022). URL <https://www.mdpi.com/2311-5521/7/10/318>.
- [21] Afkhami, S. Challenges of numerical simulation of dynamic wetting phenomena: a review. *Current Opinion in Colloid & Interface Science* **57**, 101523 (2022). URL <https://linkinghub.elsevier.com/retrieve/pii/S1359029421001072>.
- [22] Zhang, H. *et al.* Experimental study of dynamic wetting behavior through curved microchannels with automated image analysis. *Experiments in Fluids* **65**, 95 (2024). URL <https://link.springer.com/10.1007/s00348-024-03828-7>.
- [23] Szymczyk, K. & Taraba, A. Aggregation behavior of Triton X-114 and Tween 80 at various temperatures and concentrations studied by density and viscosity measurements. *Journal of Thermal Analysis and Calorimetry* **126**, 315–326 (2016). URL <http://link.springer.com/10.1007/s10973-016-5631-3>.
- [24] Rehman, N. *et al.* Surface and thermodynamic study of micellization of non ionic surfactant/diblock copolymer system as revealed by surface tension and conductivity. *J. Mater. Environ. Sci* **8**, 1161–1167 (2017).
- [25] Szymczyk, K., Zdziennicka, A. & Jańczuk, B. Effect of Polysorbates on Solids Wettability and Their Adsorption Properties. *Colloids and Interfaces* **2**, 26 (2018). URL <http://www.mdpi.com/2504-5377/2/3/26>.
- [26] Wagner, W., Kretzschmar, H.-J. & Span, R. *VDI-Wärmeatlas*, Ch. D2 Stoffwerte von bedeutenden reinen Fluiden, 175–356 (Springer Berlin Heidelberg, Berlin, Heidelberg, 2013).
- [27] Lemmon, E. W., Bell, I. H., Huber, M. L. & McLinden, M. O. *NIST Chemistry Webbook, NIST Standard Reference Database Number 69*, Ch. Thermophysical Properties of Fluid Systems, 20899 (National Institute of Standards and Technology, Gaithersburg MD, 2022). URL <https://webbook.nist.gov>.
- [28] International Association for the Properties of Water and Steam. IAPWS R1-76(2014) Revised release on surface tension of ordinary water substance (2014). URL <http://www.iapws.org/relguide/Surf-H2O-2014.pdf>.
- [29] 3M. 3MTM NovecTM 7500 Engineered Fluid (2022). URL <https://multimedia.3m.com/mws/media/65496O/3m-novec-7500-engineered-fluid.pdf>.
- [30] Schindelin, J. *et al.* Fiji: an open-source platform for biological-image analysis. *Nature Methods* **9**, 676–682 (2012). URL <https://www.nature.com/articles/nmeth.2019>.
- [31] Bradski, G. The OpenCV Library. *Dr. Dobb's Journal of Software Tools* (2000).

- [32] Fischler, M. A. & Bolles, R. C. in *Random sample consensus: A paradigm for model fitting with applications to image analysis and automated cartography* (eds Fischler, M. A. & Firschein, O.) *Readings in Computer Vision* 726–740 (Morgan Kaufmann, San Francisco (CA), 1987). URL <https://www.sciencedirect.com/science/article/pii/B9780080515816500702>.
- [33] Pedregosa, F. *et al.* Scikit-learn: Machine learning in Python. *Journal of Machine Learning Research* **12**, 2825–2830 (2011).
- [34] Hirt, C. W. & Nichols, B. D. Volume of fluid (VOF) method for the dynamics of free boundaries. *Journal of computational physics* **39**, 201–225 (1981). URL <https://www.sciencedirect.com/science/article/pii/0021999181901455>.
- [35] Roenby, J., Bredmose, H. & Jasak, H. A computational method for sharp interface advection. *Royal Society Open Science* **3**, 160405 (2016). URL <https://royalsocietypublishing.org/doi/10.1098/rsos.160405>.
- [36] Scheufler, H. & Roenby, J. Accurate and efficient surface reconstruction from volume fraction data on general meshes. *Journal of Computational Physics* **383**, 1–23 (2019). URL <https://linkinghub.elsevier.com/retrieve/pii/S0021999119300269>.
- [37] Marić, T., Kothe, D. B. & Bothe, D. Unstructured un-split geometrical Volume-of-Fluid methods – A review. *Journal of Computational Physics* **420**, 109695 (2020). URL <https://linkinghub.elsevier.com/retrieve/pii/S0021999120304691>.
- [38] OpenCFD Ltd. OpenFOAM Repository. <https://develop.openfoam.com/Development/openfoam/-/tree/OpenFOAM-v2212> (2023). Git tag OpenFOAM-v2212.
- [39] Scheufler, H. & Roenby, J. TwoPhaseFlow: An OpenFOAM based framework for development of two phase flow solvers. *arXiv preprint arXiv:2103.00870* (2021). URL <https://arxiv.org/abs/2103.00870>.
- [40] TwoPhaseFlow Repository, version of2206. <https://github.com/DLR-RY/TwoPhaseFlow/tree/of2206> (2022). Git commit: cbaf314577987db34a9e41bb4bdca511c40d080.
- [41] Denner, F. & van Wachem, B. G. Numerical time-step restrictions as a result of capillary waves. *Journal of Computational Physics* **285**, 24–40 (2015). URL <https://linkinghub.elsevier.com/retrieve/pii/S002199911500025X>.
- [42] Ganser, P., Baum, C., Chargin, D., Sauer-Budge, A. F. & Sharon, A. A practical approach for the optimization of channel integrity in the sealing of shallow microfluidic devices made from cyclic olefin polymer. *Biomedical Microdevices* **20**, 24 (2018). URL <http://link.springer.com/10.1007/s10544-018-0265-9>.
- [43] Nagy, N. Capillary Bridges on Hydrophobic Surfaces: Analytical Contact Angle Determination. *Langmuir* **38**, 6201–6208 (2022). URL <https://pubs.acs.org/doi/10.1021/acs.langmuir.2c00674>.

- [44] Albert, E. *et al.* Robust Contact Angle Determination for Needle-in-Drop Type Measurements. *ACS Omega* **4**, 18465–18471 (2019). URL <https://pubs.acs.org/doi/10.1021/acsomega.9b02990>.
- [45] Ahrens, J., Geveci, B. & Law, C. *Visualization Handbook*, Ch. ParaView: An End-User Tool for Large Data Visualization, 717–731 (Elsevier Inc., Burlington, MA, USA, 2005). URL <https://www.sciencedirect.com/book/9780123875822/visualization-handbook>.
- [46] Asghar, M. H., Fricke, M., Bothe, D. & Maric, T. Numerical wetting benchmarks – advancing the plicRDF-isoAdvector unstructured Volume-of-Fluid (VOF) method. *arXiv preprint arXiv:2302.02629* (2023). URL <https://arxiv.org/abs/2302.02629>.
- [47] Gerlach, F., Hartmann, M., Hussong, J. & Tropea, C. Rivulets of finite height. *Colloids and Surfaces A: Physicochemical and Engineering Aspects* **616**, 126012 (2021). URL <https://linkinghub.elsevier.com/retrieve/pii/S0927775720316058>.
- [48] Thammanna Gurumurthy, V. *et al.* Forced wetting in a square capillary. *Physical Review Fluids* **7**, 114002 (2022). URL <https://link.aps.org/doi/10.1103/PhysRevFluids.7.114002>.